10.48047/jocaa.2024.33.06.140

Optimization of Thrust Coefficient in Baseline and Ribbed Convergent–Divergent Nozzles

Kunal Pansari [1*], Ajay Kumar Verma[2], Vikas Kumar Sukhdeve [3], D. N. Dewangan [4]
[1]*Research Scholar, Department of Mechanical Engineering, Rungta College of Engineering and Technology, Bhilai, (C.G.), India*
[2]*Associate Professor and Head, Department of Mechanical Engineering, Shri Shankaracharya Technical Campus, Bhilai (C.G.), 490020, India*
[3]*Head, Department of Mechanical Engineering, Govt. Polytechnic, Korba, (C.G.) India*
[4]*Principal, Krishna Vikash Institute of Technology, (C.G.) India*

Abstract

This study investigates the aerodynamic performance and optimization of four convergent–divergent (C–D) rocket nozzles RN–1 (baseline), RN–2 (circular rib), RN–3 (isosceles rib), and RN–4 (scalene rib) using Computational Fluid Dynamics (CFD) and Taguchi-based design of experiments (DOE). The thrust coefficient (CF) is adopted as the primary response parameter to quantify the combined effects of internal flow expansion, wall turning, and rib-induced flow regulation. Each nozzle geometry was modeled parametrically in ANSYS Fluent under steady, compressible, axisymmetric conditions using the SST k–ω turbulence model. Three geometric factors—throat diameter (304–404 mm), convergent half-angle (28°–32°), and divergent half-angle (10°–20°)—were evaluated at three levels through an L9 orthogonal array, generating nine test cases per design. Signal-to-noise ratio and response surface analyses were employed to identify the most influential parameters and optimal settings for maximizing C_F. Simulation results show that C_F decreases with increasing throat diameter due to reduced expansion ratio, while moderate wall and divergence angles enhance exit pressure recovery. Among the tested configurations, the circular-rib nozzle RN–2 exhibited the highest $C_F = 1.813$ at Dt = 304 mm, $\theta = 30°$, $\beta = 15°$, representing the most efficient aerodynamic configuration. The scalene-rib design RN–4 followed closely with $C_F = 1.651$, benefitting from asymmetric vortex generation that stabilized shocks at higher expansion ratios. The baseline RN–1 and isosceles-rib RN–3 yielded lower C_F values, indicating limited shock control. Confirmation tests showed less than 3 % deviation from predictions, validating the model accuracy. Overall, rib integration particularly circular ribs significantly improve thrust efficiency by enhancing boundary-layer reattachment and reducing flow separation. The study demonstrates that Taguchi-based CFD optimization offers an efficient and accurate framework for nozzle design, enabling improved thrust performance with minimal computational cost.

Keywords: C-D Nozzle; Thrust Coefficient; CFD; Ribbed Nozzles; Taguchi; Optimization.

1. Introduction

Coefficient of Thrust remains a compact, outcome-level metric that collapses momentum and pressure thrust into a single efficiency figure, so studies increasingly pair it with design-of-experiments to connect geometry, operating point, and flow physics. Foundational Taguchi resources and early applications demonstrated how orthogonal arrays and signal-to-noise logic expose dominant factors with few runs, first in manufacturing processes and tribology, then in thermo-fluid components [1-3], [5]. This methodology migrated to aerospace/energy systems, where Taguchi or Taguchi-grey schemes guided multi-factor aerodynamic or thermal optimization in UAV platforms, photovoltaic-thermal layouts, and passive separators, establishing practical playbooks for factor screening and robust set-point selection under constrained budgets [3-5] [9-10]. On the nozzle side, contemporary CFD studies map how internal contours, secondary inlets, and additive-manufactured hardware alter expansion, shock topology, and wall loading; cumulative evidence shows CF sensitivity to throat/area ratios, curvature, and surface integrity (wear) across regimes from laboratory Laval nozzles to multi-inlet combustor feeds [12, 15], [17-18]. Taguchi-based aerodynamic optimization has been applied directly to complex serpentine/nozzle ducting, quantifying factor effects and robust settings for loss reduction and pressure recovery, a template that translates to rocket CD geometry tuning as well [20]. Recent experimental/numerical work reinforces that hardware realities AM tolerances, exit wear, and installation effects—shift separation/reattachment behavior and thus CF, arguing for DOE-driven tolerance bands and maintenance-aware designs [8], [17-18]. Beyond isolated nozzles, allied literature on ejectors, supersonic separators, and swirl/segmented devices shows that compressibility, phase change, and mixing control drive performance envelopes; here again, DOE and reduced-order surrogates accelerate traverse of large design spaces while CFD

10.48047/jocaaa.2024.33.06.140

resolves shock/condensation kinetics that govern losses [6], [13-14, 19], [26, 28], [31, 33]. Multi-physics campaigns—from hydrogen-rich stream separation to energy-sector supersonic units—highlight the importance of coupling thermodynamics with geometry factors to stabilize shocks and manage nonequilibrium condensation, directly impacting effective CF in integrated systems [6], [26 – 27, 33]. Process-optimization studies in adjacent domains (injection molding, machining) strengthen the statistical toolkit, combining Taguchi with PSO or RSM to reach high-quality optima and provide confirmation tests—patterns that mirror best practice in nozzle CF optimization workflows [16], [21, 24 – 25], [29 – 30, 32]. Materials/thermal papers add a durability lens (surface modification, coatings, heat-transfer constraints), reminding that wall temperature, roughness, and coating integrity feedback into boundary-layer stability, shock anchoring, and net thrust coefficients over life-cycle operation [22 – 23], [31]. Overall, the trajectory is clear: pair high-fidelity CFD for shock/separation physics with Taguchi-style DOE (and grey/RSM hybrids) for rapid factor screening and robust setting selection; validate on AM or production hardware mindful of wear/tolerance drift; and extend to coupled devices (ejectors/separators) where mixing and phase change co-determine CF. The most recent CD-nozzle study exemplifies this integrated path, using a Taguchi framework to realize measurable CF gains in a rocket application and offering a replicable confirmation-test template for future nozzle programs [12, 15], [17-18, 20], [34].

The primary objective of this research is to optimize the performance of convergent–divergent (C–D) rocket nozzles by maximizing the thrust coefficient (C_F) using Computational Fluid Dynamics (CFD) and the Taguchi design of experiments (DOE) approach. The study aims to analyze the influence of key geometric parameters: throat diameter, convergent half-angle, and divergent half-angle on nozzle performance for four different configurations: baseline (RN–1), circular-rib (RN–2), isosceles-rib (RN–3), and scalene-rib (RN–4). By systematically varying these parameters within an orthogonal array, the work seeks to identify the most significant factors affecting C_F, evaluate the aerodynamic benefits of rib integration, and determine the optimal geometric combination that yields the highest thrust efficiency. The ultimate goal is to establish a robust and validated optimization framework that combines CFD and statistical methods for efficient design and performance enhancement of rocket nozzles.

2. Materials and Methods

This study employed a computational approach to assess and optimize the thrust coefficient (CF) of four convergent–divergent (C–D) nozzle configurations—RN-1 (baseline), RN-2 (circular rib), RN-3 (isosceles rib), and RN-4 (scalene rib). All designs share the same basic convergent–throat–divergent contouring strategy; the ribbed variants introduce a passive internal feature downstream of the throat that perturbs boundary-layer growth and recompression. These levels produce a $3 \times 3 \times 3$ grid of candidate operating points; for each RN, nine representative runs (1 9) covering the factor cube are simulated to seed the Taguchi. Geometric details such as rib height, thickness, spacing, leading/trailing edge radii, and placement relative to the throat are held constant within each RN to isolate the effect of (D_t, θ, β). All drawings are parameterized so that changing D_t, θ, or βupdates the profile and rib positions without manual re-modeling errors.

2.1 Geometric Modeling

The computational domain for each nozzle was constructed of a typical convergent–divergent contour around its central axis to form an axisymmetric solid model. Each design variant (RN-1 to RN-4) follows the same overall contraction–throat–expansion profile, while the ribbed models incorporate distinct rib geometries downstream of the throat to modulate boundary-layer separation and shock interactions. RN-2 employs circular ribs, RN-3 uses isosceles-triangular ribs, and RN-4 integrates scalene-triangular ribs to assess the effect of rib asymmetry on internal flow behavior. All geometric parameters were precisely defined and constrained to ensure slope continuity at each junction and to avoid over-constraint of the surface profile. The contour dimensions and variable parameters are shown in Table 1, which specifies the convergent diameter (D_i = 1000 mm), divergent diameter (D_e = 861 mm), and variable parameters including throat diameter (Dt = 304 – 404 mm), convergent half-angle (θ = 28° – 32°), and divergent half-angle (β = 10° – 20°). Rib dimensions such as radius, base, height, and apex angle were maintained constant within each nozzle family to isolate the aerodynamic influence of the primary geometric parameters.

10.48047/jocaaa.2024.33.06.140

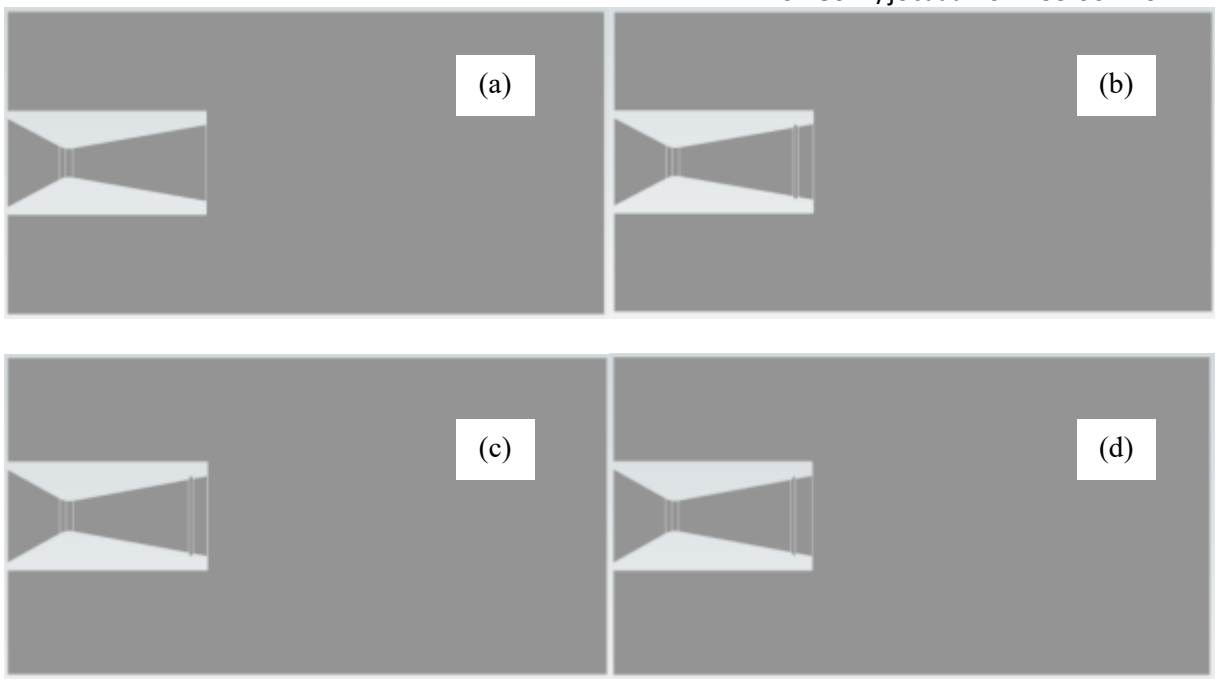

Figure 1. Computational domain (not to scale) used for the (a) RN – 1 (b) RN – 2 (c) RN – 3 (d) RN – 4 modified C-D nozzles (symmetry centerline, no-slip walls, far-field outlet)

Table 1. Geometric specification of the C–D nozzle (Bukhari et al., (2025)

Design parameter	Symbol	Dimension(s)	Type
Convergent diameter (mm)	D_i	1000	Constant
Divergent diameter (mm)	D_e	861	Constant
Throat diameter (mm)	D_t	304, 354, 404	Variable
Convergent half-cone angle (°)	θ	28°, 30°, 32°	Variable
Divergent half-cone angle (°)	B	10°, 15°, 20°	Variable
Throat fillet radius (mm)	R_f	228	Constant
Convergent length (mm)	L_c	-	Variable
Divergent length (mm)	L_d	-	Variable
Overall length (mm)	L	-	Derived
Rib radius (mm)	r	25	Constant
Triangle (Isosceles/ Scalene) rib base (mm)	b	50	Constant
Triangle (Isosceles/ Scalene) rib height (mm)	h	50	Constant
Triangle (Scalene) rib angle (°)	α	45°	Constant

2.2 Meshing

A two-dimensional, axisymmetric, structured quadrilateral grid was generated using mapped-face meshing with edge biasing toward the contraction, throat, and initial divergent section. The far-field region was graded smoothly to minimize numerical reflections while keeping the element aspect ratio within acceptable limits for compressible internal flows. of the density-based solver and boundary-insensitive exit-plane integrals. Figures 2 (a)-(c) illustrate the mesh at three levels: full domain (Figure 2(a)), internal passage (Figure 2(b)), and a throat close-up (Figure 2(c)). The grid used for the baseline solutions contains 46,509 nodes and 45,815 elements.

10.48047/jocaaa.2024.33.06.140

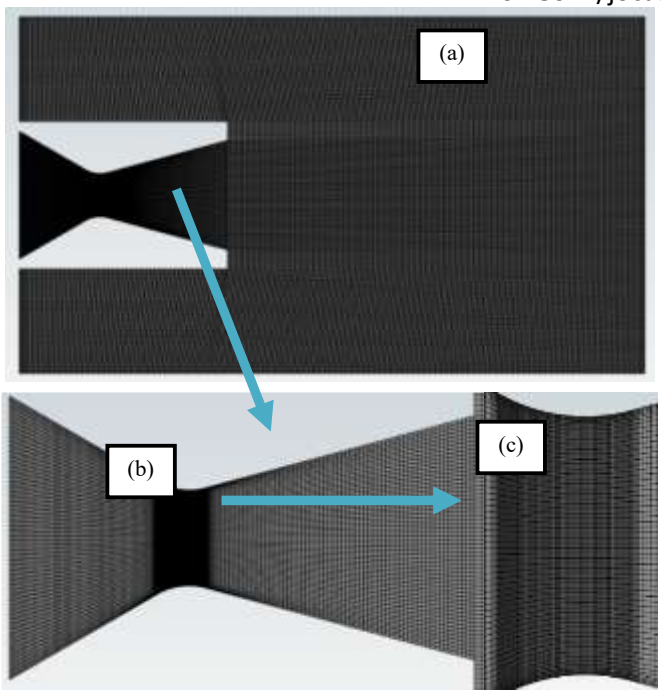

Figure 2. Computational mesh for the RN – 1 C–D nozzle: (a) full 2-D domain with downstream refinement block; (b) close-up of the throat showing clustering across the C–D junction; (c) boundary-layer refinement along the divergent wall and near rib locations

2.3 Flow Domain Preparation and Boundary Conditions

The flow domain was generated by subtracting the nozzle solid from a rectangular enclosure that carries both the internal passage and the immediate near-field plume (Figure 3). The enclosure provides an upstream settling length ahead of the convergent entry and a long downstream buffer to decouple the internal solution from outlet reflections. In practice, the inlet plane is placed about three inlet diameters upstream of the contraction, the outlet plane about ten exit diameters downstream of the lip, and the lateral clearance of the external region about eight exit diameters, which suppresses artificial confinement of the jet. The thermodynamic boundary-condition set is summarized in Table 2, confirming the use of ideal-gas air as the working fluid at standard atmospheric reference pressure. The simulation control parameters are given in Table 3, indicating that the steady-state density-based solver in ANSYS Fluent with the SST k–ω turbulence model was employed. The residual convergence criterion was set at 1×10^{-6} RMS for all governing equations, and 1500 iterations were sufficient for convergence in each run. This setup ensured numerical stability, accurate shock resolution, and consistent thrust computation at the exit plane.

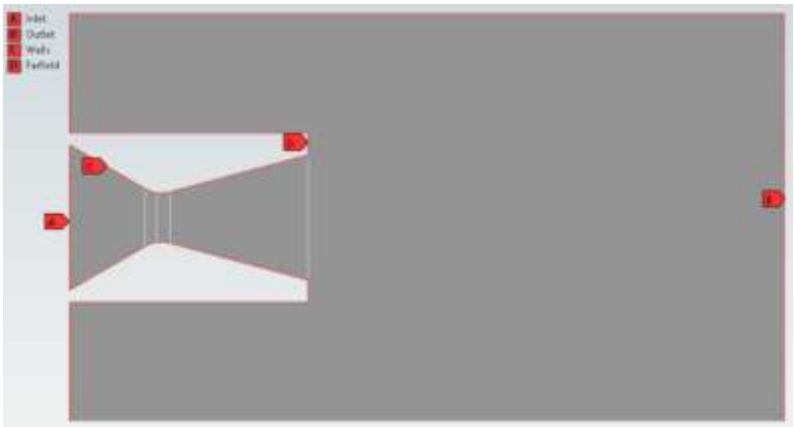

Figure 3. Boundary conditions

10.48047/jocaaa.2024.33.06.140

Table 2. Thermodynamic boundary-condition set used in CFD simulations

Parameter	Value / Type
Fluid type	Air (ideal gas)
Reference pressure	101325 Pa
Inlet (stagnation) pressure p0	9.8 MPa
Inlet (stagnation) temperature T0	3500 K
Outlet (static) pressure pb	101325 Pa

Table 3. Simulation criteria for CFD solution

Parameter	Value/Type
Solver type	CFD Fluent (Steady-State)
Turbulence model	Shear Stress Transport (SST)
Boundary condition (inlet)	Pressure Inlet (9.8 MPa, 3500 K)
Boundary condition (outlet)	Supersonic Flow, 101325 Pa
Wall condition	No-slip walls
Residuals	1×10−6 RMS
Iterations	1500

2.4 Simulation Results

A systematic design of experiments (DOE) was formulated using an L9 orthogonal array to analyze the effect of the three primary geometric parameters—throat diameter (Dt), convergent half-angle (θ), and divergent half-angle (β)—each at three levels. This configuration required nine simulation runs for each of the four nozzle designs (RN-1 to RN-4), enabling balanced estimation of main effects and interactions with a manageable number of cases. The coded levels of the three factors are shown in Table 4, corresponding to the low (−1), medium (0), and high (+1) settings. The resulting simulation data for CF at each experimental run are reported in Tables 5–8 for RN-1 through RN-4, respectively. For RN-1 (Table 5), CF values ranged from 1.355 to 1.482, indicating that performance decreases with increasing throat diameter and divergence angle. RN-2 (Table 6) demonstrated the highest thrust coefficient among all designs, with a maximum CF = 1.813 at Dt = 304 mm, θ = 30°, and β = 15°. RN-3 (Table 7) exhibited trends similar to the baseline, confirming moderate gains at lower throat diameters, while RN-4 (Table 8) achieved a maximum CF = 1.667 at the upper level of divergent angle, highlighting how scalene ribs effectively control shock losses at higher expansion ratios. These simulation results provided the quantitative foundation for subsequent Taguchi-based optimization and analyses.

.

Table 4. Coded levels of input parameters for response surface design showing three-factor variation

Factor	Symbol	Level		
		–1	0	+1
Throat Diameter (mm)	D_t	304	354	404
convergent half-angle (°)	θ	28	30	32
divergent half-angle (°)	β	10	15	20

Table 5. L_9 orthogonal array and corresponding simulated thrust coefficient (C_F) results for baseline nozzle RN – 1 under varying geometric parameters

Run	D_t	θ	β	C_F
1	304	28	10	1.482
2	304	30	15	1.463
3	304	32	20	1.481
4	354	28	10	1.414
5	354	30	15	1.408
6	354	32	20	1.402
7	404	28	10	1.372
8	404	30	15	1.358
9	404	32	20	1.355

10.48047/jocaa.2024.33.06.140

Table 6. L_9 orthogonal array and corresponding simulated thrust coefficient (C_F) results for baseline nozzle RN – 2 under varying geometric parameters

Run	D_t	θ	β	C_F
1	304	28	10	1.535
2	304	30	15	1.813
3	304	32	20	1.735
4	354	28	10	1.653
5	354	30	15	1.594
6	354	32	20	1.575
7	404	28	10	1.533
8	404	30	15	1.499
9	404	32	20	1.465

Table 7. L_9 orthogonal array and corresponding simulated thrust coefficient (C_F) results for baseline nozzle RN – 3 under varying geometric parameters

Run	D_t	θ	β	C_F
1	304	28	10	1.482
2	304	30	15	1.464
3	304	32	20	1.481
4	354	28	10	1.430
5	354	30	15	1.395
6	354	32	20	1.436
7	404	28	10	1.348
8	404	30	15	1.336
9	404	32	20	1.356

Table 8. L_9 orthogonal array and corresponding simulated thrust coefficient (C_F) results for baseline nozzle RN – 4 under varying geometric parameters

Run	D_t	θ	β	C_F
1	304	28	10	1.521
2	304	30	15	1.597
3	304	32	20	1.667
4	354	28	10	1.549
5	354	30	15	1.619
6	354	32	20	1.654
7	404	28	10	1.586
8	404	30	15	1.647
9	404	32	20	1.651

2.5 Optimized Using Taguchi

Taguchi's method is an effective tool for determining the effectiveness of a design by measuring the effect of input design parameters on output performance characteristics. This method was developed in the year 1940 by Dr. Genichi Taguchi, also known as "Taguchi philosophy". The main objective of this method is to enhance the fundamental functions of any product or process and thus create a flexible or adaptable design. Therefore, the Taguchi method is the most powerful and dynamic tool in the design of experimental methods. The Taguchi method is a three-stage design process that is system design, parameter design, and tolerance design. In this present work, parameter design is used to find out the nominal values of the respective process parameters. Parameter design is a systematic approach to find optimal settings for design parameters to minimize performance variability. Taguchi's method uses a statistical tool to measure performance characteristics known as the signal-to-noise (S/N) ratio and to select a design parameter to maximize the S/N ratio. tries. The signal

10.48047/jocaaa.2024.33.06.140

term represents the average value of the display characteristic and the noise term represents the variability of the display characteristic. Therefore, the S/N ratio includes both the mean and the variability of performance characteristics.

2.6 Performance Assessment Using Taguchi S/N Relationship

Taguchi's method uses a statistical tool to measure performance characteristics known as the signal-to-noise ratio (S/N) to find the optimal setting for design parameters and (S/N). N ratio) includes both the mean and the variability of performance. This method attempts to select design parameters to maximize the S/N ratio because the higher the S/N ratio, the more balanced the adoptable display quality. There are three criteria for signal-to-noise ratio which are lower is better, higher is better and nominal is better. In the present work, three responses are considered as coefficient of thrust. The coefficient of thrust should be maximized. Therefore, to calculate the S/N ratio of the coefficient of thrust, the higher is better criterion should be selected. The equation for the above criteria is given below:

Lower-is-Better Condition

$$S/N = -10\log\left(\frac{1}{n}\sum y^2\right) \tag{1}$$

Higher-is-Better Condition

$$S/N = -10\log\left(\frac{1}{n}\sum\frac{1}{y^2}\right) \tag{2}$$

Here, y is average of all observed value and n is number of observations.

It cannot use Taguchi's method to obtain a single optimal set of design parameters taking into account more than one performance characteristic. Therefore, this method is only useful for optimizing a single display characteristic. The optimization of design parameters with more than one performance characteristic remains an area of research.

3. Result and Discussion

The computational data obtained from the design of experiments were statistically analyzed using the Taguchi method to determine the influence of key geometric parameters: throat diameter (Dt), convergent half-angle (θ), and divergent half-angle (β) on the thrust coefficient (C_F) of the four C–D nozzle designs. The main objective of this section is to evaluate the contribution of each parameter, understand the interaction among factors, and validate the optimized levels predicted through the signal-to-noise (S/N) ratio analysis and confirmation tests.

3.1 Signal to Noise Ratios Analysis and Main Effect Plot

The Taguchi "larger-is-better" criterion was adopted since the performance goal is to maximize the thrust coefficient (C_F). The S/N ratios for each factor level were computed, and response tables were generated for all four designs (Tables 9 – Table 12). The associated main-effect plots are shown in Figures 4 – Figure 7, which clearly illustrate the trend of C_F variation with respect to each input parameter.

For the baseline nozzle RN–1, the S/N response table (Table 9) and plot (Figure 4) reveal that the throat diameter (D_t) exerts the most significant influence on C_F, followed by convergent and divergent half-angles. As Dt increases from 304 mm to 404 mm, C_F decreases noticeably, indicating that smaller throat areas favor higher expansion ratios and greater momentum thrust. The minor variations in θ and β suggest that flow turning and exit divergence angles have limited effect on the baseline performance due to the absence of flow-conditioning ribs.

Table 9. Response table of signal-to-noise (S/N) ratios for RN – 1 showing the effect of throat diameter (D_t), convergent half-angle (θ), and divergent half-angle (β) on thrust coefficient (C_F)

Level	D_t	θ	β
1	3.378	3.058	3.058
2	2.972	2.978	2.978
3	2.681	2.995	2.995
Delta	**0.696**	**0.079**	**0.079**

10.48047/jocaaa.2024.33.06.140

Rank	**1**	**2.5**	**2.5**

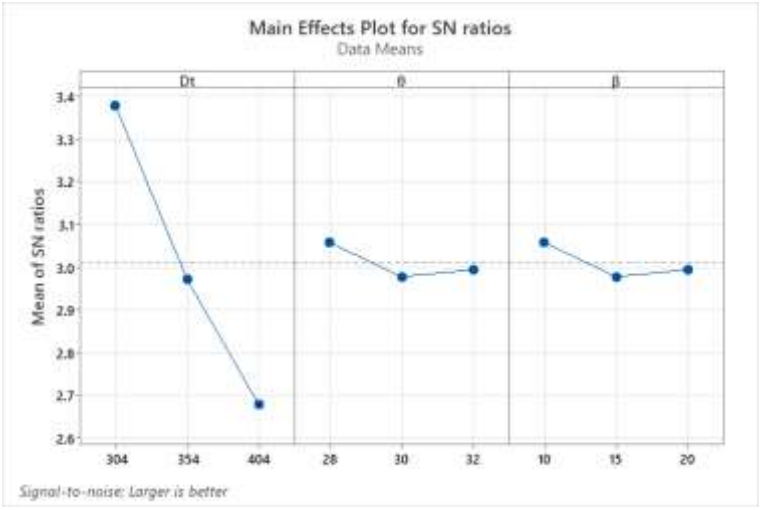

Figure 4. Main-effect plot for signal-to-noise (S/N) ratios of RN – 1 showing the dominant influence of throat diameter on thrust coefficient

Table 10. Response table of signal-to-noise (S/N) ratios for RN – 2 showing the effect of throat diameter (D_t), convergent half-angle (θ), and divergent half-angle (β) on thrust coefficient (C_F)

Level	**Dt**	**θ**	**β**
1	4.559	3.933	3.933
2	4.120	4.245	4.245
3	3.515	4.016	4.016
Delta	**1.044**	**0.312**	**0.312**
Rank	**1**	**2.5**	**2.5**

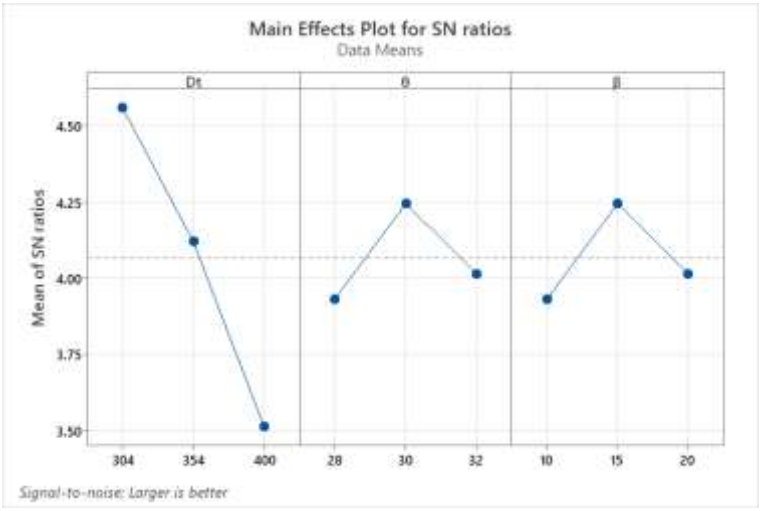

Figure 5. Main-effect plot for signal-to-noise (S/N) ratios of RN – 2 demonstrating improved CF at moderate wall and divergence angles due to circular-rib flow control

Table 11. Response table of signal-to-noise (S/N) ratios for RN – 3 showing the effect of throat diameter (D_t), convergent half-angle (θ), and divergent half-angle (β) on thrust coefficient (C_F)

Level	**Dt**	**θ**	**β**
1	3.380	3.039	3.039
2	3.047	2.906	2.906
3	2.585	3.066	3.066
Delta	**0.795**	**0.160**	**0.160**
Rank	**1**	**2.5**	**2.5**

10.48047/jocaaa.2024.33.06.140

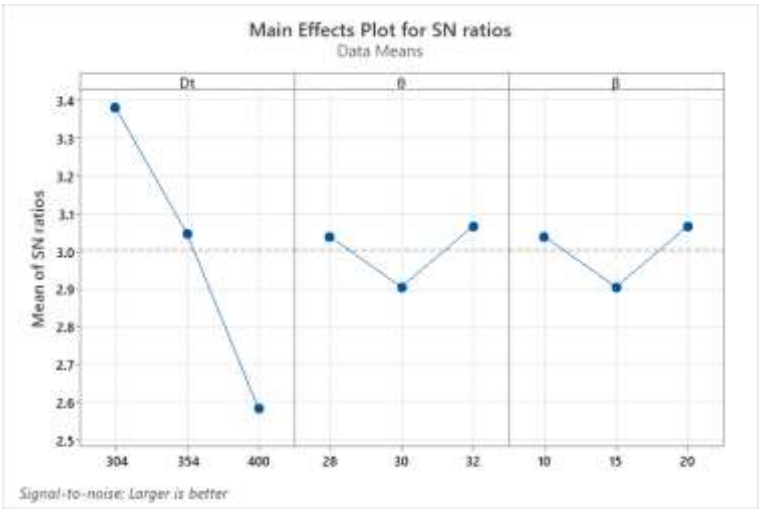

Figure 6. Main-effect plot for signal-to-noise (S/N) ratios of RN – 3 showing near-linear response trends for isosceles-rib geometry

In difference, the circular-rib nozzle RN–2 (Table 10, Figure 5) exhibits a distinctly higher C_F range, with the optimal configuration at D_t = 304 mm, θ = 30°, and β = 15°. The presence of circular ribs improves boundary-layer re-energization, suppresses separation, and stabilizes the shock pattern in the divergent section. Consequently, RN–2 records a maximum C_F = 1.813, representing the highest performance among all designs. The Δ-values in the S/N table confirm that D_t remains the most influential factor, while moderate wall and divergence angles enhance flow alignment and pressure recovery.

Table 12. Response table of signal-to-noise (S/N) ratios for RN – 4 showing the effect of throat diameter (D_t), convergent half-angle (θ), and divergent half-angle (β) on thrust coefficient (C_F)

Level	Dt	θ	β
1	4.051	3.816	3.816
2	4.119	4.196	4.196
3	4.232	4.389	4.389
Delta	**0.181**	**0.573**	**0.573**
Rank	**3**	**1.5**	**1.5**

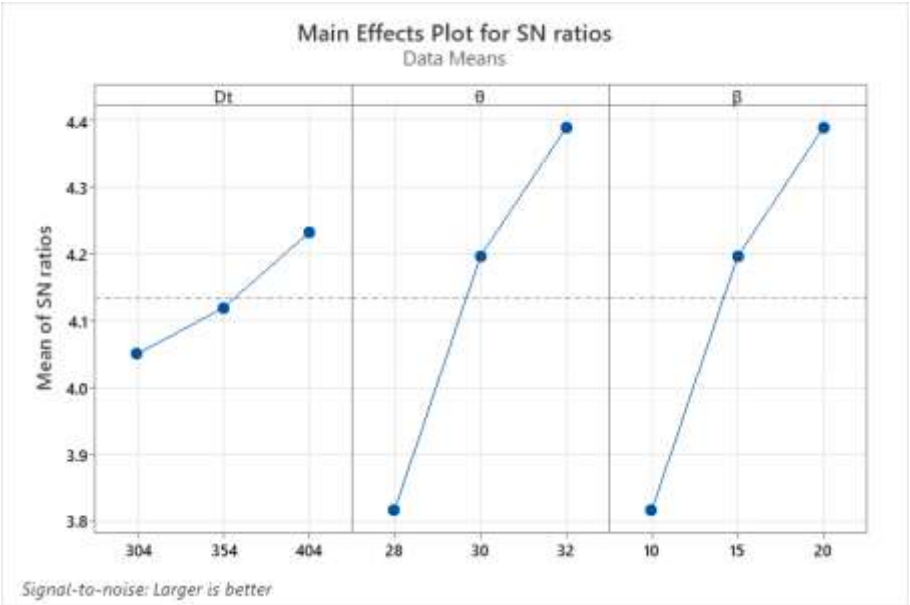

Figure 7. Main-effect plot for signal-to-noise (S/N) ratios of RN – 4 indicating strong effects of θ and β and enhanced CF at higher divergence angles

10.48047/jocaaa.2024.33.06.140

For the isosceles-rib nozzle RN–3 (Table 11, Figure 6), the CF variation resembles that of the baseline RN–1, with a slight increase at intermediate angles. The ribs induce mild flow regulation but do not create as strong a vortex-controlled reattachment as the circular ribs in RN–2. The Δ-values suggest that while throat size continues to dominate, the overall gain in C_F remains limited compared with RN–2. The scalene-rib nozzle RN–4 (Table 12, Figure 7) demonstrates a different trend. Here, both convergent and divergent angles show significant influence, while the effect of throat diameter is relatively lower. The asymmetric rib geometry promotes directional vortex formation that redistributes static pressure along the divergent wall, resulting in an increase in C_F at higher wall and divergence angles. The main-effect plot indicates an optimal C_F = 1.651, achieved at the highest β level (20°).

3.2 Interaction Plot Effects

Interaction plots for C_F variation with paired parameters are presented in Figures 8 – Figure 11 for RN–1 through RN–4, respectively. These plots depict how the influence of one factor depends on the level of another, providing insights into nonlinear coupling effects between geometric variables. For the baseline RN–1 (Figure 8), the interaction lines for Dt – θ and D_t – β remain nearly parallel, indicating minimal cross-dependency between parameters. This confirms that in the absence of ribs, C_F is primarily controlled by the throat area, and variations in wall or divergence angles have a relatively uniform influence.

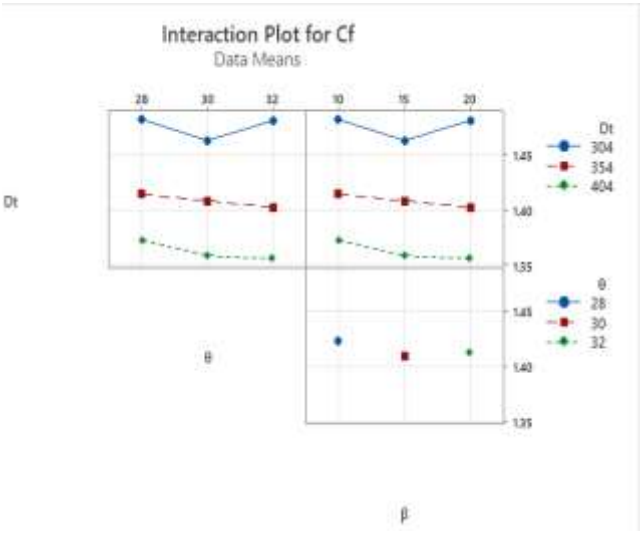

Figure 8. Interaction plot of C_F for RN – 1 illustrating minimal coupling between geometric factors and nearly parallel parameter trends

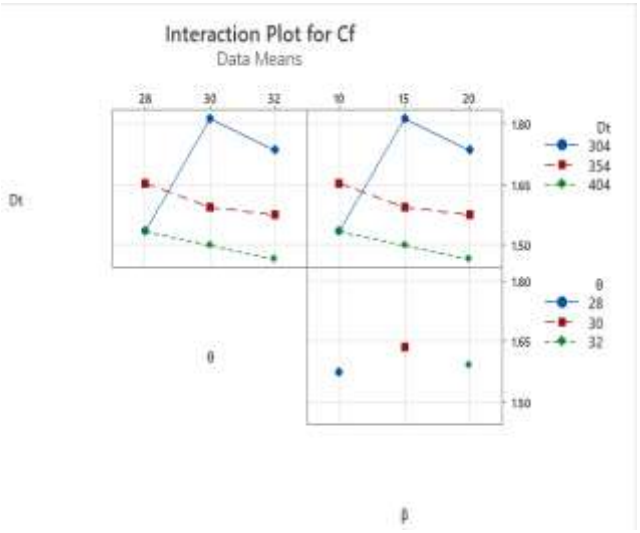

Figure 9. Interaction plot of C_F for RN – 2 revealing nonlinear interactions between D_t, θ, and β leading to maximum CF at moderate wall angles

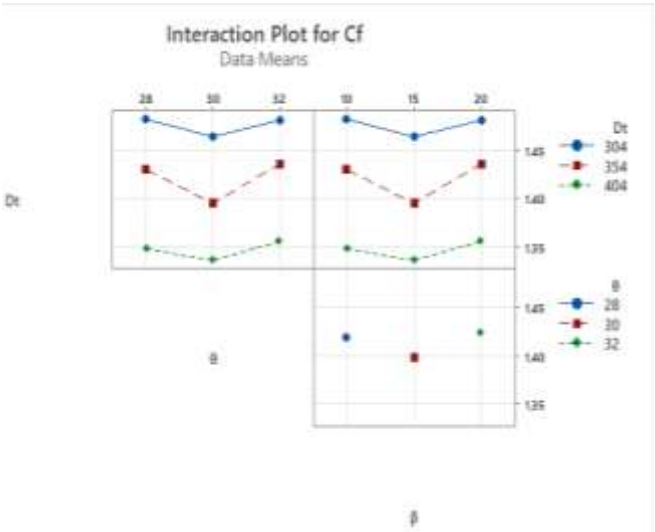

Figure 9. Interaction plot of C_F for RN – 3 displaying

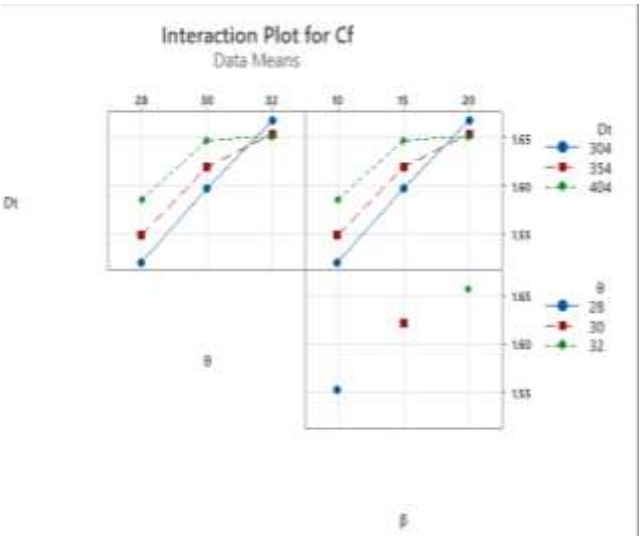

Figure 10. Interaction plot of C_F for RN – 4

10.48047/jocaaa.2024.33.06.140

weak interactions and smooth linear dependence among parameters	depicting strong θ–β coupling and asymmetric flow behavior contributing to higher thrust efficiency

In RN–2 (Figure 9), strong interactions emerge between Dt and both θ and β. The lines intersect distinctly, signifying that C_F sensitivity increases when moderate convergent angles are paired with smaller throats. The flow field benefits from the smooth curvature of the circular ribs, which create localized mixing zones that reattach the boundary layer and diminish separation losses. This interaction results in a substantial C_F improvement at the mid-angle configuration.

For RN–3 (Figure 10), the interactions are weaker and mostly linear, implying that isosceles ribs provide a balanced but limited alteration of the flow. The nearly uniform slopes of the lines show that C_F remains proportional to D_t, with little nonlinear coupling between angular parameters. The scalene-rib nozzle RN–4 (Figure 11) exhibits pronounced interaction effects, especially between θ and β. The nonparallel, intersecting trends reveal that at higher divergence angles, increasing wall inclination enhances C_F rather than reducing it a behavior attributed to asymmetric rib-induced secondary flow structures that stabilize shocks and promote smoother expansion. Hence, RN–4 demonstrates a controlled redistribution of exit pressure, achieving efficient flow at higher expansion ratios.

3.3 Optimization Level and Confirmation Test

The optimized geometric levels for maximum CF, predicted through the Taguchi approach and verified via response-surface modeling, are summarized in Table 13, while the corresponding confirmation-test results are provided in Table 14. These results quantify the accuracy of the predicted models and confirm the relative performance ranking of the four nozzle configurations.

For RN–1, the optimal combination (D_t = 304 mm, θ = 28°, β = 10°) produced a predicted C_F = 1.482 and a confirmation C_F = 1.447, corresponding to a 2.5 % deviation. The agreement validates the numerical accuracy of the baseline simulations. In RN–2, the optimized setting (D_t = 304 mm, θ = 30°, β = 15°) yielded the highest C_F = 1.813 with a 3.1 % confirmation error, confirming its superior aerodynamic performance. For RN–3, the optimized CF = 1.481 was achieved at Dt = 304 mm, θ = 32°, β = 20°, showing a 2.7 % variation, while RN–4 attained C_F = 1.651 at D_t = 404 mm, θ = 32°, β = 20° with only 2.1 % error. The small deviations between predicted and confirmation values demonstrate the robustness of the computational model and the validity of the optimization framework. Ranking the four configurations by CF reveals the order of performance as RN–2 > RN–4 > RN–1 approx. RN–3. This hierarchy highlights that circular ribs (RN–2) provide the most efficient balance of flow guidance and pressure recovery, followed by the scalene rib design (RN–4) which benefits at higher divergence angles.

Table 13. Predicted optimum levels and corresponding thrust-coefficient (C_F) values obtained from Taguchi analysis for all nozzle designs (RN – 1 to RN – 4)

RN Type	D_t (mm)	θ (°)	β (°)	C_F
RN – 1	304	28	10	**1.482**
RN – 2	304	30	15	**1.813**
RN – 3	304	32	20	**1.481**
RN – 4	404	32	20	**1.651**

Table 14. Confirmation test results for thrust coefficient (C_F) of all nozzle configurations (RN – 1 to RN – 4) comparing predicted and simulated values, with percentage error indicating model accuracy

RN Type	D_t (mm)	θ (°)	β (°)	C_F (Predicted)	C_F (Predicted-Confirmation)	% Error
RN – 1	304	28	10	**1.482**	**1.447**	**2.5%**
RN – 2	304	30	15	**1.813**	**1.758**	**3.1%**
RN – 3	304	32	20	**1.481**	**1.442**	**2.7%**
RN – 4	404	32	20	**1.651**	**1.616**	**2.1%**

4. Conclusion

The present computational study successfully examined and optimized the performance of four axisymmetric

10.48047/jocaaa.2024.33.06.140

convergent–divergent rocket nozzles using the Taguchi method with the thrust coefficient (C_F) as the response metric. The primary geometric parameters—throat diameter, convergent half-angle, and divergent half-angle—were systematically varied across nine simulation runs per configuration, yielding comprehensive insights into how flow geometry influences expansion characteristics and overall thrust performance. The results confirmed that the throat diameter (D_t) is the most influential factor affecting C_F, as smaller throats produce higher expansion ratios and more efficient momentum conversion. Convergent (θ) and divergent (β) angles have secondary yet important roles, with moderate wall turning and divergence promoting smoother pressure gradients and shock stabilization. Among the designs, the circular-rib nozzle (RN–2) achieved the highest thrust coefficient (C_F = 1.813), outperforming all other configurations. The inclusion of circular ribs effectively re-energized the boundary layer, minimized flow separation in the divergent section, and enhanced the uniformity of the exit jet. The scalene-rib nozzle (RN–4) also demonstrated improved performance at higher wall and divergence angles, confirming that asymmetric rib-induced vortices can delay shock formation and improve exit-flow stability. The baseline RN–1 and isosceles-rib RN–3 recorded relatively lower C_F values, suggesting that their flow structures lacked the same level of aerodynamic control. The Taguchi optimization framework, supported by signal-to-noise analysis and confirmation testing, validated the robustness of the numerical model, with all predicted and confirmed C_F values showing less than 3 % error. The final performance ranking RN–2 > RN–4 > RN–1 = RN–3 clearly identifies the superiority of the circular-rib geometry in achieving enhanced thrust efficiency and structural simplicity.

In conclusion, the study demonstrates that geometric rib integration is an effective passive method for improving nozzle performance without altering external dimensions or operating conditions. The approach provides a rapid, cost-effective pathway for optimizing high-speed internal flow devices using CFD and statistical design techniques. Future work may extend the analysis to include three-dimensional effects, transient flow behavior, and experimental validation to further refine the design of advanced ribbed C–D nozzles for aerospace propulsion systems.

References

[1] Shaji S, Radhakrishnan V. Analysis of process parameters in surface grinding with graphite as lubricant based on the Taguchi method. J Mater Process Technol 2003;141(1):51–9.

[2] Taguchi G, Chowdhury S, Wu Y. Taguchi's quality engineering handbook. New York: John Wiley & Sons, Inc.; 2004. p. 1602–17.

[3] Venkatesan G, Kulasekharan N, Iniyan S. Design and selection of curved vane demisters using Taguchi based CFD analysis. Desalination 2014;354:39–52.

[4] Pahange H, Abolbashari MH. Mass and performance optimization of an airplane wing leading edge structure against bird strike using Taguchi-based grey relational analysis. Chin J Aeronaut 2016;29(4):934–44.

[5] Naqiuddin NH, Saw LH, Yew MC, et al. Numerical investigation for optimizing segmented micro-channel heat sink by TaguchiGrey method. Appl Energy 2018;222:437–50.

[6] de Oliveira Arinelli L, de Medeiros JL, Teixeira AM, de Araújo OQF (2019) Modeling of supersonic separators and membrane permeation units for processing of CO2-rich natural gas with HYSYS implementation. In: Offshore Processing of CO, pp 163–213. https://doi.org/10.1007/978-3-03004006-2_6

[7] Hariram V, Seralathan S, Arunraja P, Salih Arshad A, Jaganathan R (2019) Numerical analysis on cone length and its effect on performance of an automotive catalytic converter. Int J Vehic Struct Syst 11(2):161–168

[8] Feng C et al (2020) Effect of nozzle exit wear on the fluid flow characteristics of supersonic oxygen lance. Metall Mater Trans B 51(1):187–199. https://doi.org/10.1007/S11663-019-01722-W/METRICS

[9] Kazemian A, Parcheforosh A, Salari A, et al. Optimization of a novel photovoltaic thermal module in series with a solar collector using Taguchi based grey relational analysis. Sol Energy 2021;215:492–507.

[10] Kapsalis S, Panagiotou P, Yakinthos K. CFD-aided optimization of a tactical Blended-Wing-Body UAV

10.48047/jocaaa.2024.33.06.140

platform using the Taguchi method. Aerosp Sci Technol 2021;108::106395.

[11] An S, Bang BH, Lee MW, Yoon SS (2021) Review of recent progress in the supersonic cold-spraying technique with solid ps and liquid suspensions. Exp Fluids 62(7):1–25. https://doi.org/10.1007/S00348-021-03247-Y

[12] D. Das, R. Sardar, S. Sarkar, and N. K. Manna, "Compressible Flow Through Convergent–Divergent Nozzle," in Theoretical, Computational, and Experimental Solutions to Thermo-Fluid Systems, Singapore, M. Palanisamy, V. Ramalingam, and M. Sivalingam, Eds., 2021// 2021: Springer Singapore, pp. 345-353.

[13] de Almeida Avancini B, Carmo B (2021) Numerical modeling of fluids mixture flow in high velocities with phase change. https://doi.org/10.26678/ABCM.COBEM2021.COB2021-0224

[14] Fazioli Gastaldo R, Restrepo Lozano JC, Galdino da Silva R, Marcondes Orselli R, Simões Moreira JR, Carmo B (2021) Numerical study and development of an experimental test-rig configuration of a supersonic nozzle for gas separation. https://doi.org/10.26678/ABCM.COBEM2021.COB2021-1224

[15] Bhaskar A. and M. K. Sahu, "Numerical investigation on performance of convergent–divergent nozzle with multi-inlet combustion chamber of a rocket engine," Heat Transfer, vol. 51, no. 1, pp. 5-21, 2022/01/01 2022, doi: https://doi.org/ 10.1002/htj.22296.

[16] H. Q. Ayun, J. Triyono, and E. Pujiyanto, "Optimization of injection molding simulation of bioabsorbable bone screw using Taguchi method and particle swarm optimization," Jordan Journal of Mechanical and Industrial Engineering, vol. 16, no. 2, pp. 319-325, 2022.

[17] Chen M, Baby R, Dillard S, Lee YT, Ekkad S (2022) Design and test a converging and de Laval nozzle using additive manufacturing. Front Aerosp Eng 1:951987. https://doi.org/10.3389/FPACE.2022.951987

[18] Douaiba, F. Baghlad, and M. Hamel, "Analysis of compressible flow at the outlet of a convergent – divergent nozzle," Desalination and Water Treatment, vol. 279, pp. 160-163, 2022/12/01/ 2022, doi: https://doi.org/10.5004/dwt.2022.29102.

[19] El Zohbi B, Bukharin N, Assoum HH, Abed-Meraim K, Sakout A, El Hassan M (2022) Investigation of the effects of the jet nozzle geometry and location on the performance of supersonic fluid ejectors. Energy Rep 8:228–233. https://doi.org/10.1016/J.EGYR.2022.01.029

[20] Zhang X, Shan Y, Zhang J, Wu Z. Optimization for aerodynamic performance of double serpentine nozzles with spanwise offsets using Taguchi-based CFD analysis. Chinese J. of Aeronautics 2023;36(5):1-17.

[21] H. M. Abdu, S. M. Tahaa, A. Wazeer, A. Abd El-Mageed, and M. M. Mahmoud, "Application of Taguchi Method and Response Surface Methodology on Machining Parameters of Al MMCs 6063-TiO 2," Jordan Journal of Mechanical and Industrial Engineering, vol. 17, no. 4, 2023.

[22] S. M. A. Bukhari, N. Husnain, F. A. Siddiqui, M. T. Anwar, A. A. Khosa, M. Imran, T. H. Qureshi, and R. Ahmad, "Effect of laser surface remelting on Microstructure, mechanical properties and tribological properties of metals and alloys: A review," Optics & Laser Technology, vol. 165, p. 109588, 2023/10/01/ 2023, doi: https://doi.org/10.1016/ j.optlastec.2023.109588.

[23] S. M. A. Bukhari, A. Naveed, N. Husnain, F. A. Siddiqui, M. F. Zaman, A. Ahmad, R. Ahmad, and N. Wajahat, "Computational study of mechanical behavior of Ti6Al4V coated and aluminium-coated 316L stainless steel alloy under linear and cyclic loading," Technical Journal, vol. 28, no. 03, pp. 12-24, 2023.

10.48047/jocaaa.2024.33.06.140

[24] H. M. Abdu, S. M. Tahaa, A. Wazeer, A. Abd El-Mageed, and M. M. Mahmoud, "Application of Taguchi Method and Response Surface Methodology on Machining Parameters of Al MMCs 6063-TiO 2," Jordan Journal of Mechanical and Industrial Engineering, vol. 17, no. 4, 2023.

[25] H. Alzyod and P. Ficzere, "Thermal Evaluation of Material Extrusion Process Parameters and Their Impact on Warping Deformation," Jordan Journal of Mechanical and Industrial Engineering, vol. 17, no. 4, 2023.

[26] Ding H, Zhang Y, Yang Y, Wen C (2023) A modified Euler-Lagrange-Euler approach for modelling homogeneous and heterogeneous condensing droplets and films in supersonic flows. Int J Heat Mass Transf 200. https://doi.org/10.1016/J.IJHEATMASSTRANSFER.2022.123537

[27] Han C, Jiang W, Liu Y, Dou Z, Jin B (2023) Numerical study on carbon dioxide removal from the hydrogen-rich stream by supersonic Laval nozzle. Int J Hydrogen Energy 48(38):14299–14321. https://doi.org/10.1016/J.IJHYDENE.2022.12.244

[28] Huang X, Rodriguez C, Liang Q, Wang Z, Liu Y, Ding C (2023) Performance study of a supersonic swirl separator. Processes 11(7):2218. https://doi.org/10.3390/PR11072218

[29] T. Alsardia and L. Lovas, "Investigation of the Effect of the Surface Treatment and Lubrication During Repeated Tightening on the Nut Coefficient of a Bolted Joint Using the Taguchi Method," Jordan Journal of Mechanical and Industrial Engineering, vol. 18, no. 1, 2024.

[30] H. Gowda and R. HN, "Study on Strontium and Sodium Modification Elements on Microstructure, Mechanical, Wear and Fracture Behavior of Al7075 Alloy by Taguchi Technique," Jordan Journal of Mechanical and Industrial Engineering, vol. 18, no. 1, 2024.

[31] M. F. Zaman, S. M. A. Bukhari, N. Husnain, Z. Abbas, A. Ayyub, M. F. Najmi, A. Manan, and M. Zahid, "Effect of zirconium carbide coating on thermal behavior of heavy duty V12 diesel engine using finite element method," Engineering Research Express, vol. 6, no. 2, p. 025549, 2024/05/30 2024, doi: 10.1088/2631-8695/ad4f51.

[32] T. Alsardia and L. Lovas, "Investigation of the Effect of the Surface Treatment and Lubrication During Repeated Tightening on the Nut Coefficient of a Bolted Joint Using the Taguchi Method," Jordan Journal of Mechanical and Industrial Engineering, vol. 18, no. 1, 2024.

[33] Daglish J et al (2024) A coalescing filter for liquid-liquid separation and multistage extraction in continuous-flow chemistry. Org Process Res Dev. https://doi.org/10.1021/acs.oprd.4c00012

[34] Bukhari S. M. A., b. MeraJ, N. Husnain, R. Qurashi, W. Abbas, M. T. Anwar, N. Wajahat, A. Tahir, M. F. Zaman (2025). CFD Based Design Optimization of Convergent-Divergent Nozzle of High-Speed Rocket Using the Taguchi Method for Enhanced Flow Characteristics. Jordan Journal of Mechanical and Industrial Engineering, 19 (2), 249-262, doi: 10.59038/jjmie/190201.